Secondary amine-activated ferrate(VI) for isoquinoline degradation: Relationship between molecular structure and reactive performance

Secondary Amine-Activated Ferrate(VI): Relationship Between Molecular Structure and Reactive Performance

Ying Wang [a,b], Liang Chen [a,b], Xin Chen [a,b], Shengchi Bai [c], Xiaoqi Wang [c], Wen Wen [c], Wen Liu [d], Jun Ma [e], Alberto Tiraferri [f], Baicang Liu [a,b,*]

[a] State Key Laboratory of Hydraulics and Mountain River Engineering, College of Architecture and Environment, Sichuan University, Chengdu, Sichuan, 610207, China

[b] Yibin Institute of Industrial Technology, Sichuan University Yibin Park, Section 2, Lingang Ave., Cuiping District, Yibin, Sichuan, 644000, China

[c] Research Institute of Petroleum Exploration & Development (RIPED), PetroChina, No. 20 Xueyuan Road Haidian District, Beijing, P. R. China

[d] The Key Laboratory of Water and Sediment Sciences, Ministry of Education, College of Environmental Sciences and Engineering, Peking University, Beijing 100871, China

[e] State Key Laboratory of Urban Water Resource and Environment, Harbin Institute of Technology, Harbin 150090, China

[f] Department of Environment, Land and Infrastructure Engineering, Politecnico di Torino, 10129, Turin, Italy

Corresponding author: Baicang Liu, E-mail: bcliu@scu.edu.cn; baicangliu@gmail.com

Abstract

This study systematically elucidates the electronic structure-activity relationship between secondary amines and ferrate (Fe(VI)) activation. Comparative experiments demonstrated that pyrrolidine (Py) significantly outperformed diethylamine (Di) in enhancing Fe(VI)'s oxidation capability across various dosage conditions and pollutant systems, with Py-Fe(VI) achieving approximately 7-fold higher rate constant than Fe(VI) alone for isoquinoline (IQL) degradation, versus a 2-fold improvement observed with the Di-Fe(VI) system. Mechanistic studies combining quenching experiments and EPR characterization corroborated Fe(IV)/Fe(V) as dominant reactive species for IQL degradation, with kinetic modeling revealing that Fe(IV) contributes >80% to IQL degradation in all processes. Electrochemical analyses suggested that Fe(VI) activation by Di and Py might involve the formation of iron-secondary amine complexes. Density functional theory calculations highlighted Py's lower energy barrier for Fe(VI) complexation (27.7 vs. Di's 29.1 kcal/mol), accelerating activation. Secondary amines were shown to stabilize Fe(IV) via coordination, extending its reactive lifetime. Systematic evaluation of various secondary amines revealed a significant negative correlation between the highest occupied molecular orbital energy levels of amines and Fe(VI) activation performance, indicating that moderate electron-donating capacity promotes iron complexation and pollutant degradation. This work establishes a molecular design framework for Fe(VI) activators while providing new insights into high-valent iron-mediated oxidation mechanisms, advancing sustainable water treatment strategies.

Keywords

Ferrate; Secondary amines; High-valent iron species; Kinetic model; Theoretical

calculations

Synopsis

This study established a quantitative correlation mechanism between secondary amine configuration and Fe(VI) activation efficiency.

1. Introduction

In recent years, ferrate (Fe(VI)) has attracted extensive research attention as an environmentally friendly and multifunctional water treatment agent due to its unique redox properties [1,2]. This compound combines strong oxidizing capacity with multifunctional synergistic effects [3], enabling efficient pathogen inactivation [4], organic pollutant degradation [5,6], inorganic pollutant transformation [7,8], and heavy metal ion removal [9]. Notably, it produces no halogenated disinfection by-products during treatment [10] and demonstrates superior resistance to water matrix interference compared to chlorine-based disinfectants and ozone [11]. Although Fe(VI) demonstrates multifunctional advantages, its practical implementation remains constrained by kinetic limitations in pollutant degradation compared to ozone, Fenton reagents, and other advanced oxidation processes (AOPs) [11]. Furthermore, its intrinsic instability poses critical challenges, such as rapid decomposition under acidic conditions [12,13]. These pH-dependent limitations collectively restrict its operational versatility across diverse water matrices. To address these bottlenecks, there exists an urgent demand for developing efficient Fe(VI) activation strategies while broadening its operational pH spectrum, thereby enabling more robust and adaptable water treatment applications.

Studies have demonstrated that the oxidative capabilities of highly reactive high-valent iron species (Fe(IV)/Fe(V)) markedly surpass those of Fe(VI) [1,14]. Existing research confirms that strategies including acid activation [15], coupling with carbon-based materials [2,16], synergistic oxidation [17–19], reduction agents [20–23], metal oxide catalysis [24–26], and energy field enhancement [2,27] can significantly increase the proportion of Fe(IV)/Fe(V) generation in Fe(VI) systems. Of particular interest are amine compounds, which are ubiquitous in natural water systems as reductive media derived from dissolved organic matter and anthropogenic pollutants, such as pharmaceuticals, personal care products, and pesticides [28]. Emerging studies have revealed that nitrogen-containing substances like creatinine [29], aliphatic amines [28], and amino acids [1] can activate Fe(VI) through electron transfer processes, substantially improving pharmaceutical pollutant degradation efficiency. Notably, the amine functional groups in pharmaceuticals play a decisive role in governing their oxidative transformation pathways mediated by Fe(VI). This structural dependence is particularly evident in sulfonamide antibiotics, where the electronic and steric properties of amine moieties dictate the selectivity of oxidation intermediates and final products [30]. A critical distinction lies in the activation mechanisms among primary, secondary, and tertiary aliphatic amines: secondary amines exhibit optimal enhancement effects by preferentially generating Fe(IV)-dominated active species, while structurally unique amines, e.g., proline, achieve efficient pollutant removal via Fe(V)-mediated pathways.

To systematically elucidate the structure-activity relationship between amine configurations and Fe(VI) activation mechanisms, this study selects diethylamine (Di, Figure 1a) and pyrrolidine (Py, Figure 1b) as model compounds. Despite their similar molecular weights and chemical compositions, Di possesses a flexible aliphatic chain structure, whereas Py features a rigid cyclic configuration. This structural difference provides an ideal comparative system for investigating the impact of molecular rigidity on Fe(VI) activation efficiency. The research focuses on four key objectives: (1)

comparing the differential enhancement effects of Di and Py on Fe(VI)-mediated degradation of pollutants; (2) identifying critical active species (radical/non-radical) and quantifying their contributions; (3) elucidating molecular mechanisms underlying Fe(VI) activation by different amines; (4) establishing quantitative structure-activity relationships between secondary amine configurations nd Fe(VI) activation efficiency to provide guidance for designing high-performance Fe(VI) activators. This work not only advances fundamental understanding of Fe(VI)-amine interactions but also offers scientific foundations for developing ligand-regulated advanced water treatment technologies.

2. Materials and Methods

2.1. Chemicals and Reagents

All the chemicals and reagents used were at least analytical grade; detailed descriptions are provided in the Supporting Information (SI), Text S1. The synthesis procedure for potassium ferrate (Fe(VI)) is presented in Text S2 of the SI

2.2. Experiment Procedures

All batch degradation experiments were conducted at 25 ± 1 ºC in glass beakers on a magnetic stirrer (300 rpm). Each pollutant was individually added to the 100 mL system at a concentration of 10 μM. The reaction was initiated by simultaneously adding the target amount of amine compounds and solid Fe(VI). The pH was maintained at 9.0 ± 0.05 with 10 mM borate buffer. At predetermined time intervals, a 1 mL sample was collected and immediately quenched with excess hydroxylamine hydrochloride (100 μL of 0.1 M $NH_2OH{\cdot}HCl$), and then filtered (0.22 μm) into UPLC vials before analysis. Other experiments under different conditions also followed the above procedures. All experiments were performed in at least duplicates and the results are presented as average data with one standard deviation.

2.3. Analytical Methods

The pH values were monitored with a pH meter (FE-28, Mettler Toledo, USA). The measurement of Fe(VI) concentration is detailed in Text S3 Measurements of micropollutant concentrations are described in Text S4 and Table S1. Electron paramagnetic resonance (EPR) analysis is presented in Text S5. Electrochemical tests were conducted in a three-electrode electrochemical cell (Text S6).

2.4. Theoretical calculations

Structure optimizations were carried out with Gaussian 16, Revision A.03 package [31] at the B3LYP [32,33] level of theory including Grimme's D3 dispersion corrections with Becke-Johnson damping (D3BJ) [34,35] with a def2SVP basis set [36–39]. To identify each stationary point as either an energy minimum or a transition state, analytical frequency calculations were carried out at the same level of theory. On the basis of the gas-phase optimized structures, single point energy values were calculated using the B3LYP functional with a def2-TZVP basis set [36–39]. All reported energies are based on gas-phase Gibbs free energies for which the electronic energies were corrected to B3LYP with def2-TZVP basis set and solvent effects. The calculation of the Fukui index for Di and Py molecule was performed using the Multiwfn software [40] (details shown in Text S7).

2.5. Kinetic Modeling

The program Kintecus V6.51 (www.kintecus.com) was used for kinetic fitting and simulation for IQL oxidation in the Fe(VI) alone, Di-Fe(VI), and Py-Fe(VI) systems. The reaction equations employed in the kinetic model are displayed in Tables S2−S4, and the models were validated by the model sensitivity analysis (Texts S8−S10 and

Figures S10−S19)[41].

3. Results and Discussion

3.1. Oxidation Performance of secondary amine-Fe(VI)

The degradation of isoquinoline (IQL) by individual systems (Di alone, Py alone, Fe(VI) alone) and combined systems (Di-Fe(VI), Py-Fe(VI)) was systematically investigated. As shown in Figure S1, neither Di nor Py alone exhibited any IQL degradation capability within 300 seconds of reaction. In contrast, the Fe(VI) alone, Di-Fe(VI), and Py-Fe(VI) systems achieved IQL removal efficiencies of 40.9%, 66.1%, and 90.1%, respectively. As depicted in Figure 1c, all the three processes followed second-order kinetics. The rate constants for Di-Fe(VI) and Py-Fe(VI) were determined to be 7.73 $M^{-1}s^{-1}$ and 25.7 $M^{-1}s^{-1}$, respectively, representing approximately 2-fold and 7-fold enhancements compared to the sole Fe(VI) process (3.69 $M^{-1}s^{-1}$). It is obvious that the introduction of Di or Py significantly enhanced the Fe(VI)-mediated degradation of IQL.

Additionally, the degradation of 12 micropollutants were systematically evaluated with Di alone, Py alone, Fe(VI) alone, Di-Fe(VI), and Py-Fe(VI) processes. The target contaminants included: antibiotics, i.e., sulfamethoxazole (SMX), tetracycline (TET), ciprofloxacin (CIP); endocrine disruptors, i.e., bisphenol A (BPA, atrazine (ATZ), dimethyl phthalate (DMP); pharmaceuticals, i.e., diclofenac (DCF), carbamazepine (CBZ), ibuprofen (IBU); representative organics in shale gas wastewater, i.e., IQL, 6-Methylquinoline (6-MQ), indoline (IDL) (see Figure S2 and Figure 1d). Within 300 s, Di and Py alone exhibited negligible degradation for all tested micropollutants. Fe(VI) achieved partial degradation of 9 out of 12 contaminants within 5 minutes, with the exceptions of DMP, IBU, and ATZ, likely because Fe(VI) typically exhibits high reactivity toward electron-rich contaminants but inertness toward electron-deficient ones [27]. Notably, except for DMP, TET, BPA, and IDL, the latter three having already achieved 100% degradation by Fe(VI) alone, the addition of Di and Py enhanced the degradation of all tested micropollutants. Py consistently exhibited a stronger catalytic enhancement than Di, with this phenomenon observed across different pollutant categories, implying the broad applicability of the observed catalytic behavior.

The dosage-dependent effects of secondary amines on IQL degradation were evaluated in Di-Fe(VI) and Py-Fe(VI) processes. As shown in Figures 1e–f, increasing the Di or Py concentrations from 10 to 40 μM initially enhanced IQL degradation efficiency, followed by a slight decline at 50 μM. This phenomenon likely arised from excessive Di or Py reducing high-valent iron species (Fe(VI)/Fe(V)/Fe(IV)) to less reactive lower-valence states (Fe(III)/Fe(II)), which commonly exhibit diminished oxidative capacity for IQL degradation. Notably, Py exhibited persistent catalytic superiority over Di across all tested dosages under identical experimental conditions, thereby emphasizing the reproducibility and mechanistic stability of this enhancement phenomenon. Investigations into additional influencing parameters (e.g., pH, coexisting ions) are provided in Figures S3–S4 and Text S11–S12.

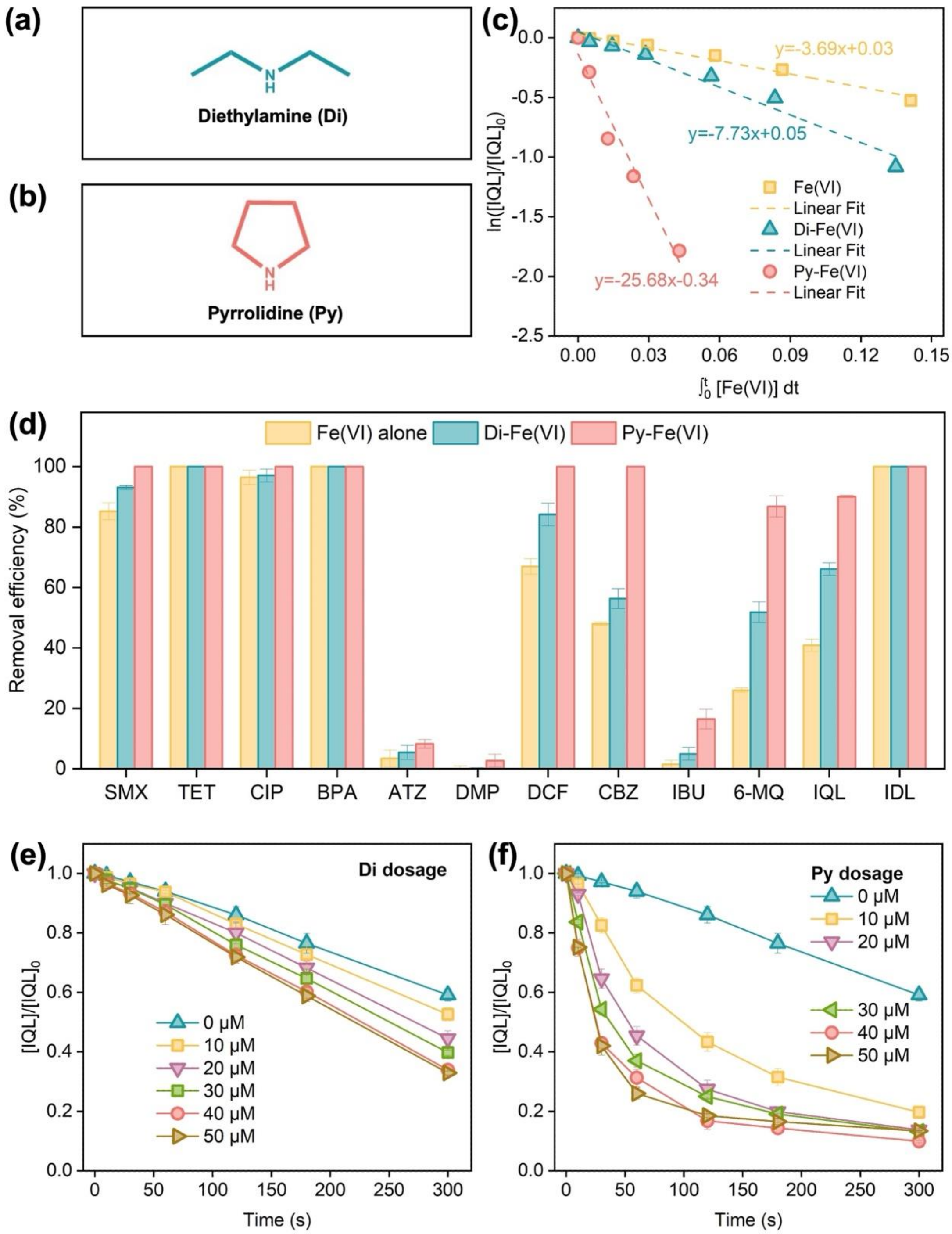

Figure 1. Structural formula of Di (a) and Py (b); Degradation kinetics of IQL by Fe(VI), Di-Fe(VI), and Py-Fe(VI) processes (c); Removal of various pollutants by Fe(VI) alone, Di-Fe(VI), and Py-Fe(VI) processes (d); Effect of Di dosage (e) and Py dosage (f) on IQL removal. Experiment conditions: pH = 9.0, $[IQL]_0$ = 10 μM, $[Di]_0$ = $[Py]_0$ = 40 μM, $[Fe(VI)]_0$ = 500 μM.

3.2. Evidence for the Fe(V)/Fe(IV) Contribution

To examine the possible reactive oxygen species (ROS, e.g., $HO^{\bullet}$, $O_2^{\bullet-}$, and $^1O_2$) and reactive iron species (Fe(IV)/Fe(V)) for IQL depletion during the Fe(VI)-based processes, a combination of EPR spectroscopy, quenching tests, and probe compounds was utilized (Text S13). As depicted in Figure 2a, $HO^{\bullet}$ was likely not involved in any of the processes, scine no signal of the DMPO-$HO^{\bullet}$ adduct was observed. The role of $HO^{\bullet}$ was also ruled out using the probe compound nitrobenzene (NB) [42,43], as NB had no effect on the removal of IQL (Figure 2b), and no removal of NB was observed in these systems (Figure S5). Then, to identify the role of $O_2^{\bullet-}$, CCl_4 was chosen as a scavenger for $O_2^{\bullet-}$, since CCl_4 is relatively reactive with $O_2^{\bullet-}$ (1.1×10^9 M^{-1} s^{-1})[44,45]. The presence of 50 mM CCl_4 showed a negligible inhibition on the abatement of IQL, indicating that $O_2^{\bullet-}$ did not have substantial involvement in any of the systems, with or without secondary amines (Figure 2b and Figure S6). The employment of nitro blue tetrazolium (NBT) as a characteristic probe also ruled out the role of $O_2^{\bullet-}$, because the absorbance of NBT could not be reduced (Figure S7) and there was no characteristic absorption peak of NBT-$O_2^{\bullet-}$ at 560 nm[46] (Figure S8). Furthermore, visible light-rose bengal (Vis-RB) process, a classical system that only produces $^1O_2$ [47], was conducted to verify the role of $^1O_2$. As summarized in Figure S9, the Vis-RB process did not lead to the degradation of IQL, reflecting that the $^1O_2$ was not responsible for IQL elimination. Although a TEMP-$^1O_2$ signal was observed (Figure 2c), it may not be attributed to $^1O_2$, a mechanism that will be discussed below. The results collectively excluded the significant roles of ROS in IQL removal. In other words, active iron species oxidation should be the largely main mechanism responsible for removing IQL within the Fe(VI), Di-Fe(VI), and Py-Fe(VI) systems.

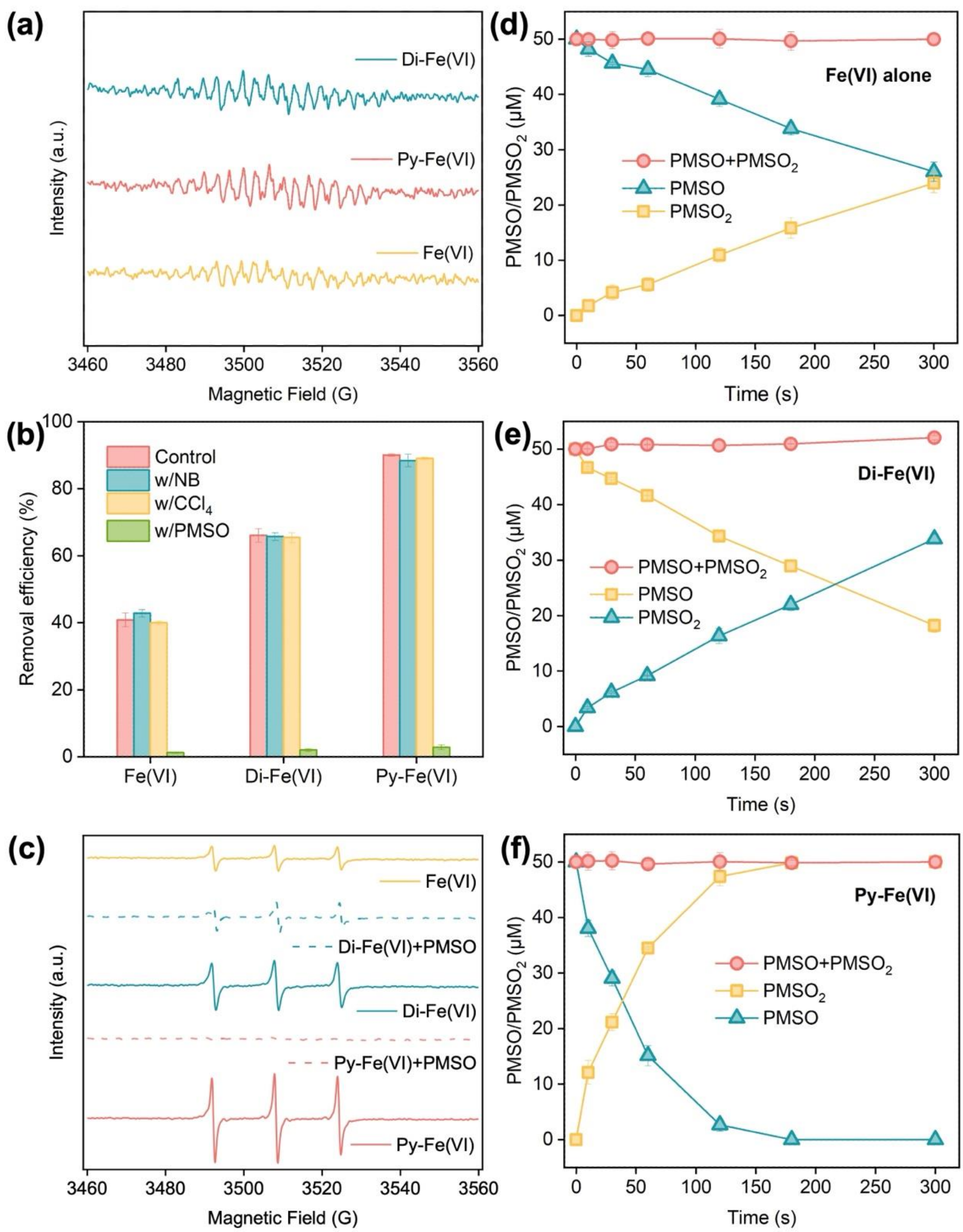

Figure 2. EPR spectra of DMPO-HO$^{\bullet}$ in various processes (a); Influence of different scavengers and probes on the removal of IQL by Fe(VI) alone, Di-Fe(VI), and Py-Fe(VI) processes (b); EPR spectra of TEMP-$^{1}O_2$ in various processes (c); Degradation of PMSO and generation of $PMSO_2$ in Fe(VI) alone (d), Di-Fe(VI) (e), and Py-Fe(VI) (f) processes. Experiment conditions: pH = 9.0, $[IQL]_0$ = 10 μM, $[Di]_0$ = $[Py]_0$ = 40 μM, $[Fe(VI)]_0$ = 500 μM, $[PMSO]_0$ = 1 mM, $[NB]_0$ = 10 μM, $[CCl_4]_0$ = 50 mM.

It is well known that methyl phenyl sulfoxide (PMSO) can be oxidized by high-valent iron (Fe(IV)/Fe(V)) into $PMSO_2$ through oxygen-atom transfer pathway, which observably differs from the radical-based oxidation pathway, during which PMSO mainly transforms into other products, such as hydrolyzed PMSO[16,48]. Typically, Fe(IV)/Fe(V) exhibits higher oxidation capability than Fe(VI) with PMSO. Thus, PMSO has been frequently used to check the formation of Fe(IV)/Fe(V) in Fe(VI)-based oxidation processes. When 1 mM of PMSO was added into Fe(VI), Di-Fe(VI), and Py-Fe(VI) systems, the removal performance of IQL was remarkably restrained (Figures 2b). For instance, when 1 mM PMSO was added to the reaction solution, only 1.24%, 2.03%, and 2.84% of IQL abatement was obtained after 300s treatment for Fe(VI) alone, Di-Fe(VI), and Py-Fe(VI), respectively, while 40.9%, 66.1%, and 90.1% IQL removal was achieved by the corresponding three processes in the absence of PMSO. The obvious suppression phenomenon of IQL degradation may be attributed to PMSO and IQL competing for Fe(IV)/Fe(V). This also suggested that Fe(IV)/Fe(V) played a dominant role in IQL removal.

Furthermore, the degradation of PMSO by sole Fe(VI), Di-Fe(VI), and Py-Fe(VI) processes was explored. As reflected in Figures 2d–2f, the proportion of generated $PMSO_2$ to degraded PMSO consistently remained around 100% throughout the entire reaction sequence, demonstrating that nearly all PMSO degradation was converted into $PMSO_2$ through the oxygen transfer mechanism in all processes. The findings additionally confirm that the involvement of radicals may be considered negligible, with Fe(V) and Fe(IV) being identified as the key reactive species responsible for the removal of IQL. Importantly, compared with sole Fe(VI) process, Di-Fe(VI) and Py-Fe(VI) processes achieved faster degradation of PMSO and formation of $PMSO_2$, which is attributed to the addition of Di and Py speeding up the generation of

Fe(IV)/Fe(V). Figure 2c presents the EPR spectrum of TEMP-$^1O_2$ in various processes: a signal for the TEMP-$^1O_2$ adduct was observed in the Fe(VI) alone process, while the signals for adduct in the Di-Fe(VI) and Py-Fe(VI) systems were significantly stronger than that of the Fe(VI) alone. Previous research has reported that high-valent iron (Fe(IV), Fe (V), Fe(VI)) could lead to false positives in $^1O_2$ EPR detection[49]. Therefore, the signals here were likely attributed to high-valent iron, since with the presence of PMSO the signals were significantly reduced. The enhanced signal in Di-Fe(VI) and Py-Fe(VI) process also indicated that the production of Fe(IV)/Fe(V) was increased. In summary, Fe(V)/Fe(IV) was likely the dominant reactive species for IQL removal in the Di-Fe(VI) and Py-Fe(VI) reaction processes.

3.3. Identification of Fe(IV)/Fe(V)/Fe(VI) Contribution to IQL degradation

The results discussed above corroborate that only Fe(IV), Fe(V), and Fe(VI) were involved in IQL oxidation. However, the specific contributions of ferrates in this process are still unknown. Thus, a model was built based on major reactions (details in Tables S2–S4) and employed to fit the kinetics of IQL degradation by Kintecus software. Based on the modeled results, Fe(V) and Fe(IV) contributed 18.6% and 80.3% to IQL oxidation in the Fe(VI) alone process, respectively. Fe(IV) was the dominant reactive species for IQL degradation in the Di-Fe(VI) process (86.4% contribution), while the contribution of Fe(V) was 12.9%. Similarly, Fe(IV) accounted for 92.5% of the IQL oxidation in the Py-Fe(VI) process, whereas Fe(V) contributed only 7.48% to IQL oxidation. Of note is that the contribution of Fe(IV) obviously increased in the Di-Fe(VI) and Py- Fe(VI) processes, in comparison with that of the sole Fe(VI) system (Figures 3), suggesting the role of Fe(IV). The above models were tested with a sensitivity analysis and model validation (Figures S10–S18) and the results confirmed that the fitting results were valid. Furthermore, the concentration profiles of ferrates in Fe(VI) alone, Di-Fe(VI), and Py-Fe(VI) were also determined based on the simulation. Figure S19 shows that the concentration of Fe(IV) was about three orders of magnitude higher than that of Fe(V) during IQL degradation by three different processes. Note that the concentration of Fe(IV) in the Di-Fe(VI) and Py-Fe(VI) processes were increased compared with the case of Fe(VI) alone, suggesting the increased amounts of reactive species under the activation of Di and Py. In general, the results strongly suggest that Fe(IV) played a dominant role in all the three processes.

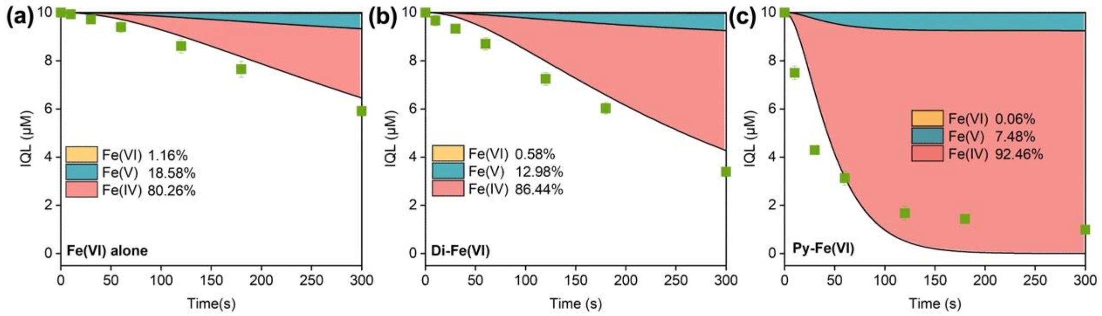

Figure 3. Contributions of Fe(IV), Fe(V), and Fe(VI) to IQL degradation by Fe(VI) alone (a), Di-Fe(VI) (b), and Py-Fe(VI) (c) processes.. Experiment conditions: pH = 9.0, $[IQL]_0$ = 10 μM, $[Di]_0$ = $[Py]_0$ = 40 μM, $[Fe(VI)]_0$ = 500 μM.

3.4. Activation Mechanism of Fe(VI) by Secondary Amines and Corresponding Theoretical Calculations

As mentioned above, both Di and Py enhanced the oxidative performance likely by activating Fe(VI) to generate Fe(IV)/Fe(V) intermediates. In this process, Fe(VI) acts as an electron acceptor, while Di and Py serve as electron donors. This section will delve into the specific activation sites of Fe(VI) by Di and Py, along with the relevant functional groups, through DFT calculations. Figure 4a, 4c, 4f, and 4h illustrates the distribution of negative and positive electrostatic potentials around Di and Py using a gradient from blue to red. The deep blue regions represent areas of concentrated negative charge, surrounding N atoms, which correlate with stronger affinity for high-valent Fe active species and greater potential for chemical activation. By analyzing the electron density isosurface maps of f^-, f^+, and f^0 on the surfaces of Di and Py, it is evident that the -NH groups in Di and Py are expected to exhibit higher reactivity (Figure S20). While the isosurface mapping of electron density provides intuitive insights, it does not facilitate detailed quantitative analysis of Fukui function values. To enable a more streamlined and intuitive interpretation, a simplified version of the Fukui function was employed to predict the sites in Di and Py molecules that are susceptible to attack by reactive species. The condensed Fukui function theory indicates that larger f^-, f^+, and f^0 values correspond to atoms more prone to electrophilic, nucleophilic, and radical attacks, respectively. The 3N site in Di and the 1N site in Py display the highest f^- values (Figure 4d–4e), suggesting these locations are likely the first to be targeted by Fe(VI).

The highest occupied molecular orbital (HOMO) is a critical indicator reflecting the electron-donating capacity of a molecule. Figure 4b and 4g reveals that the HOMOs of both Di and Py were apt to be localized on the -NH groups. Thus, the electrons in the -NH groups of Di and Py are readily delocalized. The HOMO value of Py (−6.36 eV) is more negative than that of Di (−6.09 eV), indicating that Di has superior electron-donating capability to Fe(VI) compared to Py. This observation, which exhibits an inverse correlation with the degradation trend of IQL, will be analyzed in subsequent sections.

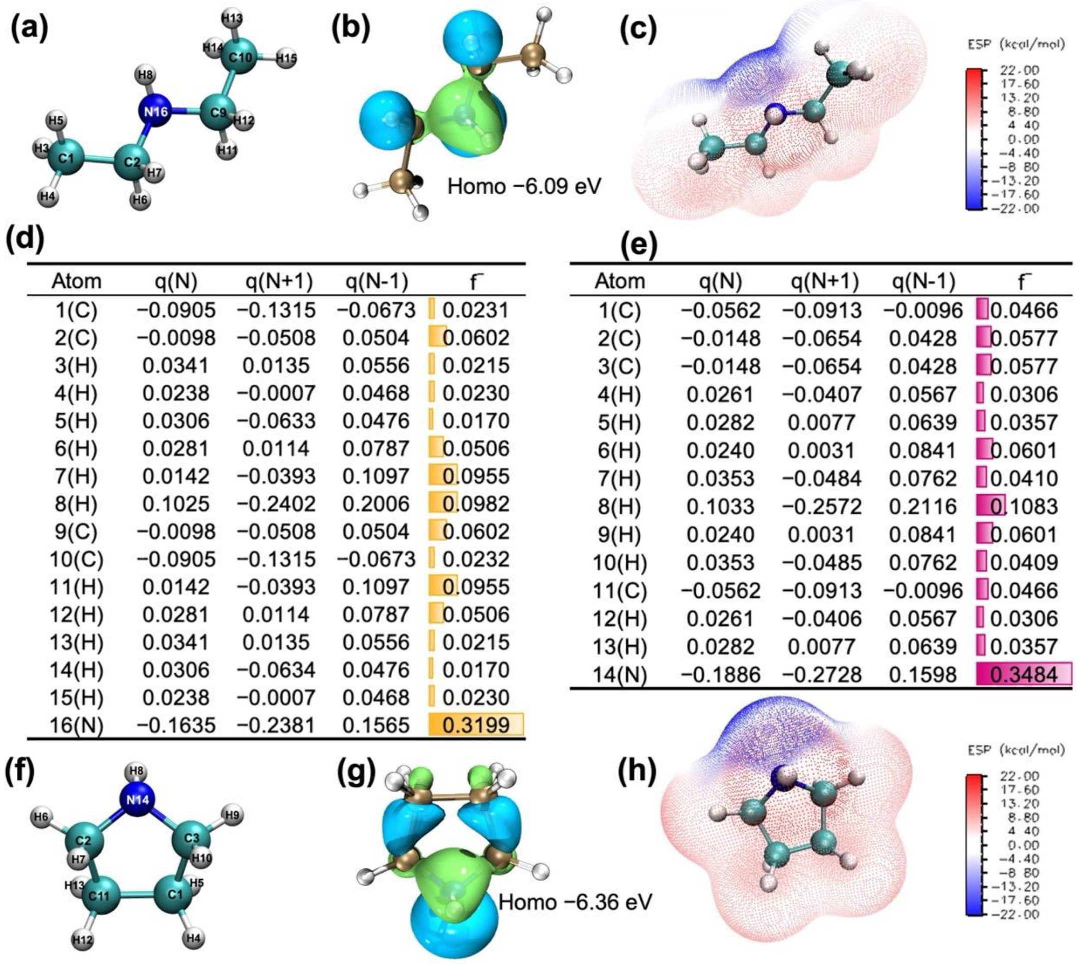

(d)

Atom	q(N)	q(N+1)	q(N-1)	f⁻
1(C)	−0.0905	−0.1315	−0.0673	0.0231
2(C)	−0.0098	−0.0508	0.0504	0.0602
3(H)	0.0341	0.0135	0.0556	0.0215
4(H)	0.0238	−0.0007	0.0468	0.0230
5(H)	0.0306	−0.0633	0.0476	0.0170
6(H)	0.0281	0.0114	0.0787	0.0506
7(H)	0.0142	−0.0393	0.1097	0.0955
8(H)	0.1025	−0.2402	0.2006	0.0982
9(C)	−0.0098	−0.0508	0.0504	0.0602
10(C)	−0.0905	−0.1315	−0.0673	0.0232
11(H)	0.0142	−0.0393	0.1097	0.0955
12(H)	0.0281	0.0114	0.0787	0.0506
13(H)	0.0341	0.0135	0.0556	0.0215
14(H)	0.0306	−0.0634	0.0476	0.0170
15(H)	0.0238	−0.0007	0.0468	0.0230
16(N)	−0.1635	−0.2381	0.1565	0.3199

(e)

Atom	q(N)	q(N+1)	q(N-1)	f⁻
1(C)	−0.0562	−0.0913	−0.0096	0.0466
2(C)	−0.0148	−0.0654	0.0428	0.0577
3(C)	−0.0148	−0.0654	0.0428	0.0577
4(H)	0.0261	−0.0407	0.0567	0.0306
5(H)	0.0282	0.0077	0.0639	0.0357
6(H)	0.0240	0.0031	0.0841	0.0601
7(H)	0.0353	−0.0484	0.0762	0.0410
8(H)	0.1033	−0.2572	0.2116	0.1083
9(H)	0.0240	0.0031	0.0841	0.0601
10(H)	0.0353	−0.0485	0.0762	0.0409
11(C)	−0.0562	−0.0913	−0.0096	0.0466
12(H)	0.0261	−0.0406	0.0567	0.0306
13(H)	0.0282	0.0077	0.0639	0.0357
14(N)	−0.1886	−0.2728	0.1598	0.3484

Figure 4. Chemical structure of Di (a) and Py (f); Highest occupied molecular orbital (HOMO) of Di (b) and Py (g); Electrostatic potential (ESP) distribution of Di (c) and Py (h); Natural population analysis (NPA) charge distributions and condensed Fukui index (f^-) of Di (d) and Py (e).

3.5. Coordination between Fe(VI) and Secondary Amines

In-situ electrochemical analysis was further used to investigate the promoting mechanism of Di-Fe(VI) and Py-Fe(VI) processes. Figure 5a shows the variation curve of the open circuit potential with time, using a mercury oxide electrode (HgO) as the reference electrode and Pt sheet electrodes as the working and counter electrodes. After Fe(VI) was added to the solution, the potential rose immediately from initial 0.68 V to final 0.83 V after stabilization. Because Fe(VI) is a strong oxidizing agent, the addition of Fe(VI) enhanced the oxidizing power, resulting in a higher potential. After the subsequent addition of Di or Py, the potential began to decrease, indicating that Di and Py acted as reductants in the reaction, donating electrons and reducing Fe(VI) to low-valent forms, such as Fe(IV) and Fe(V). Next, the residual Fe(VI) concentrations for Fe(VI) alone, Di-Fe(VI), and Py-Fe(VI) processes were investigated (Figure 5b). After 300 s reaction time, the value of $[Fe(VI)]/[Fe(VI)]_0$ ratio was 0.94, 0.90, and 0.58 in the sole Fe(VI), Di-Fe(VI), and Py-Fe(VI) systems, respectively, indicating that the consumption of Fe(VI) could be remarkably improved with the presence of Di and Py. The consumption of Fe(VI) was effectively improved by Di and Py, while the Di-Fe(VI) and Py-Fe(VI) processes still showed higher performance for IQL abatement than sole Fe(VI). As a whole, these results indicate that more reactive species, such as active high-valent iron intermediate species, (Fe(IV), Fe(V)), may be formed by the combination of Di and Py with Fe (VI) [14,28].

Cyclic voltammetry (CV) measurements were conducted for the three systems (Figure 5c). Redox peaks were observed in all three systems; given the limited electrochemical data for Fe(VI) in the existing literature, it is hypothesized that the observed reduction may correspond to the reductive conversion of high-valent Fe species to low-valent forms, such as Fe(IV) and Fe(V). The Py-Fe(VI) process exhibited the highest peak current, indicating the presence of more active iron species in the process. It is noteworthy that, compared to the Fe(VI) alone, both the Di-Fe(VI) and Py-Fe(VI) processes exhibited a positive shift in oxidation peaks and a negative shift in reduction peaks in their CV curves. This phenomenon could be attributed to the coordination of Di and Py with Fe(VI) to form complexes, where the complexation altered the redox potential of Fe(VI). The negative shift in reduction peaks indicates that the Fe(VI) complexes are more easily reduced than free Fe(VI), suggesting a lowering of their reduction energy barrier. Furthermore, electrochemical impedance spectroscopy (EIS) was employed to evaluate the charge transfer resistance of the catalysts during redox reactions [50] (Figure 5d). A lower Tafel slope indicates higher intrinsic activity and reduced transport limitations [51]. The order of the semicircle radii in the Nyquist plots was: Fe(VI) < Di-Fe(VI) < Py-Fe(VI), with Py-Fe(VI) process showing the largest radius. This phenomenon is due to the coverage of the electrode surface by the complexes after their formation, leading to an increase in resistance. These results validate the hypothesis discussed above: taken together, the efficacy of Di and Py in activating Fe(VI) for IQL removal appears to be influenced by their coordination properties.

To elucidate the superior activation performance of Py over Di in enhancing Fe(VI)-mediated IQL degradation and unravel the mechanistic origins of differential Fe(V)/Fe(IV) contribution ratios, we conducted density functional theory (DFT) calculations to compare the reaction energy barriers of the various systems. Thermodynamic parameters for reactants, transition states (TS), intermediates, and products in Di- and Py-Fe(VI) reaction systems are summarized in Tables S7–S9, with Gibbs free energies illustrated in Figures 5e and 5f. The results indicate that the activation energy barrier for Py to form transition state TS1 with Fe(VI) (27.7 kcal/mol) is lower than that of Di (29.1 kcal/mol), implying faster reaction kinetics for Py. This observation aligns with the enhancement trend discussed in Section 3.1, which suggested that Py-Fe(VI) exhibited superior IQL degradation compared to Di-Fe(VI). This phenomenon may arise from the conformational rigidity of Py's cyclic structure, which facilitates optimal geometric alignment for hydrogen abstraction and oxygen transfer processes. Concurrently, intracyclic orbital conjugation and favorable lone-pair electron orientation within the pyrrolidine ring may synergistically promote Fe-O bond cleavage while stabilizing O-N bond formation. Although Di is characterized by a marginally lower TS2 barrier (13.5 vs. 14.0 kcal/mol for Py), the decisive TS1 disparity may govern the overall reaction kinetics, establishing Py's superiority.

Furthermore, we note that the energy barrier for the formation of complex int2 between Py and Fe(VI) (12.9 kcal/mol) was found to be lower than the corresponding value for Di (14.5 kcal/mol), indicating that Py should coordinate more efficiently with Fe(VI). During the reaction between Py and Fe(VI), the energy barrier for the formation of complex int4 between Fe(IV) and Py(O) (13.0 kcal/mol) was also found to be lower than the corresponding value for Di (13.9 kcal/mol), suggesting that the Fe(IV)-Py(O) complex should be more stable and may effectively inhibit its conversion into less reactive Fe(II)/Fe(III). Based on Tables S2–S4, Fe(V) in all three systems is primarily generated from the reaction between Fe(VI) and Fe(II). Consequently, the Fe(IV) contribution in the Py-Fe(VI) system is higher than that in the Di-Fe(VI) system, while the Fe(V) contribution is lower. Overall, Py may provide superior advantages in intermediate formation and stabilization, further supporting its kinetic dominance.

In summary, the findings discussed here suggest that the enhanced pollutant degradation performance of secondary amines (e.g., Di, Py) with Fe(VI) is closely related to their ability to form stable complexes with high-valent iron species (Fe(VI)/Fe(IV)/Fe(V)). Notably, differences in coordination capacity are hypothesized to directly determine the superiority or inferiority of the resulting catalytic performance.

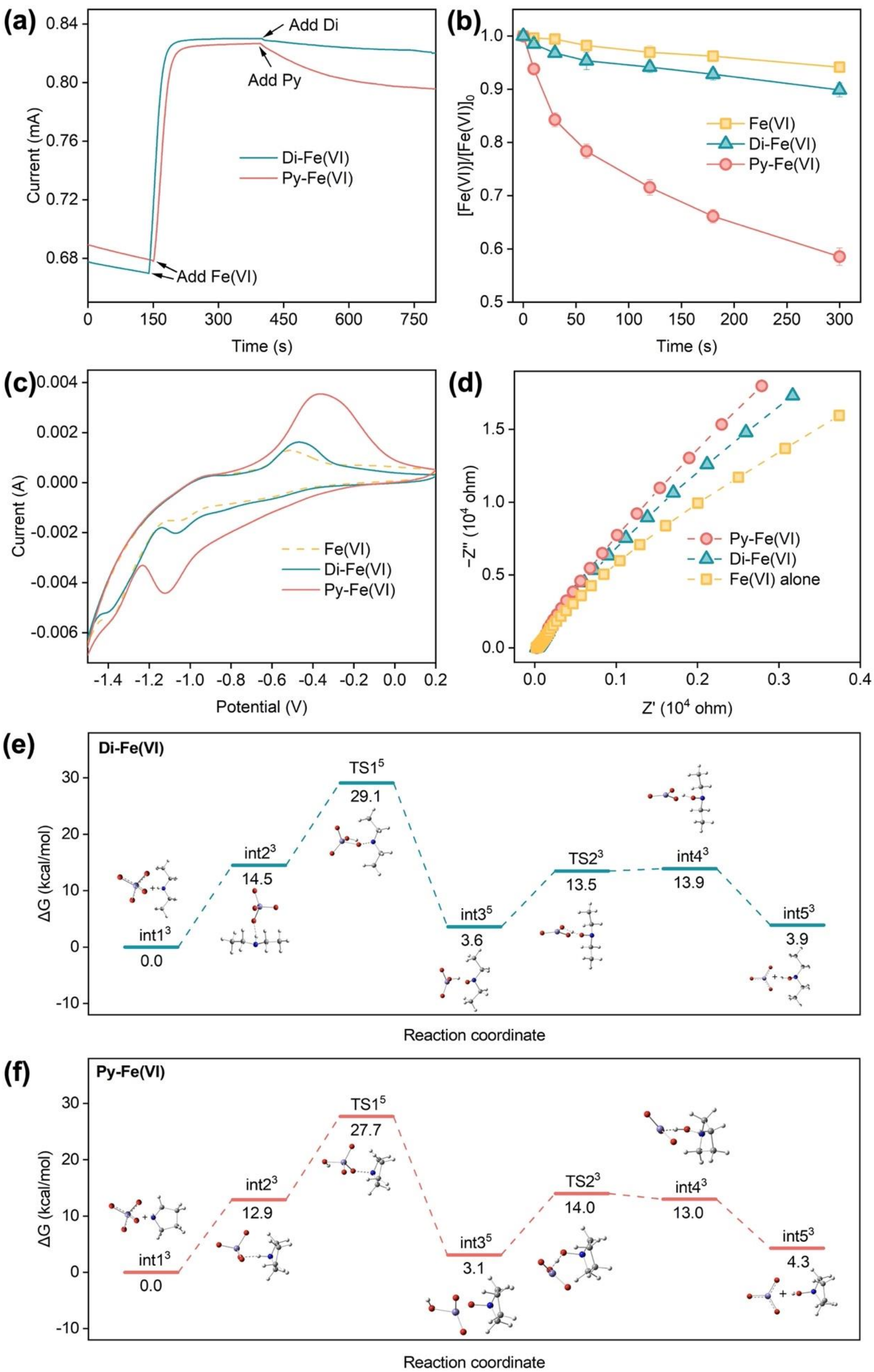

Figure 5. Change of open-circuit potential in Di-Fe(VI) and Py-Fe(VI) processes (a);

Decomposition of Fe(VI) in reaction solution with or without Di and Py (b); Cycle voltammetry measurements of Fe(VI), Di-Fe(VI), and Py-Fe(VI) processes (c); EIS measurements of Fe(VI), Di-Fe(VI), and Py-Fe(VI) processes (d); Gibbs free energy pathway between Di and Fe(VI) (e), Py and Fe(VI) (f). Experiment conditions: pH = 9.0, $[IQL]_0$ = 10 μM, $[Di]_0$ = $[Py]_0$ = 40 μM, $[Fe(VI)]_0$ = 500 μM.

3.6. Structure Effects of Secondary Amine

The regulatory effects of seven structurally distinct secondary amines was investigated in the Fe(VI)-mediated degradation of isoquinoline (IQL). The tested amines included five linear secondary amines: dimethylamine (DMA), Di, dibutylamine (DBA), diisopropylamine (DIPA), and N-ethylisopropylamine (EIPA), along with two cyclic secondary amines, namely, Py and piperidine (PIP). Among the linear amines, DMA, Di, and DBA possess straight-chain alkyl groups, whereas DIPA and EIPA feature branched structures (Figure 6a). Results indicated that DMA, Di, DBA, and Py enhanced Fe(VI)- mediated IQL degradation, with efficacy following the order: Py > DMA > Di > DBA (Figure 6b). Notably, the cyclic amine Py exhibited superior activation performance compared to linear amines, likely attributed to its rigid molecular structure facilitating stable complexation with Fe(VI). Such coordination may effectively stabilize reactive iron intermediates. In linear amine systems, shortening the alkyl chain length improved activation efficiency, highlighting the critical role of steric hindrance, with longer chains hindering optimal coordination. However, DIPA, EIPA, and PIP inhibited degradation. This anomaly may arise from unique steric effects imposed by their branched structures or electronic interference with Fe(VI) redox processes.

Although preliminary comparisons between Di and Py showed a positive correlation trend between their coordination ability with Fe(VI) and IQL removal efficiency, directly quantifying the coordination capabilities of various secondary amines with Fe(VI) faces significant challenges. Coordination strength is influenced by multiple factors, including solvent effects, steric hindrance, and dynamic reaction conditions, which complicate precise measurement or quantitative estimation. [52]. In contrast, the HOMO energy levels (E_{HOMO}) calculated via quantum chemical methods should offer a stable theoretical measure of the intrinsic electron-donating properties of amines. Moreover, as discussed in Sections 3.4 and 3.5, there appears to be a theoretical relationship between E_{HOMO} and coordination ability: higher E_{HOMO} values were associated with weaker coordination. Based on this premise, we investigated the correlation between IQL removal and E_{HOMO} values for seven secondary amines. Quantum chemical calculations revealed a significant negative correlation between IQL degradation and the E_{HOMO} levels (Figure 6c, Figure S21). This finding suggests that the electron-donating capacity of secondary amines inversely correlates with their coordination ability. Effective Fe(VI) activation requires moderate electron-donating capacity: excessive electron donation (high HOMO levels) may trigger over-reduction of Fe(VI) to Fe(II)/Fe(III), prematurely depleting its oxidative potential.

In summary, this study suggests that the electron-donating capacity of secondary amines exhibits a negative correlation with Fe(VI) activation, thus providing theoretical guidance for designing high-performance Fe(VI) activators, while also unveiling the intricate relationships between ligand electronic properties and oxidant activation mechanisms.

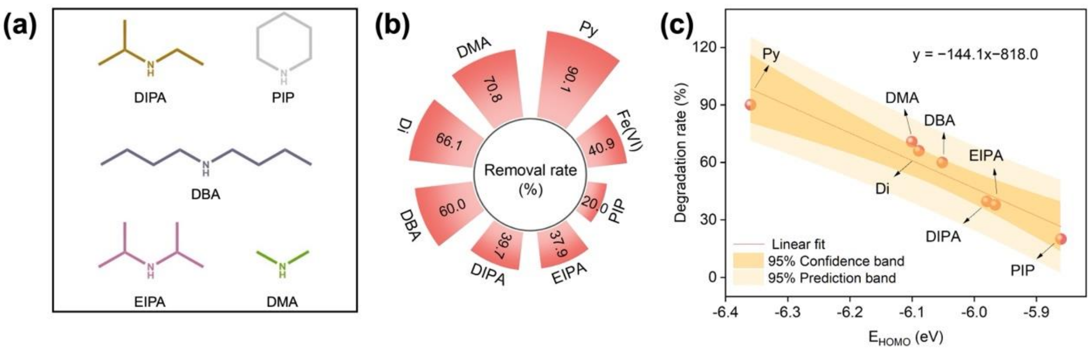

Figure 6. Chemical stucture of DIPA, PIP, DBA, EIPA, and DMA (a); Degradation efficiencies of IQL by Fe(VI) with and without secondary amines (b); Correlation between the HOMO energy levels (E_{HOMO}) and IQL degradation rate (c); HOMO and LUMO of Py, Di, DIPA, PIP, DBA, EIPA, and DMA (d). Experiment conditions: pH = 9.0, $[IQL]_0$ = 10 μM, [secondary amines]$_0$ = 40 μM, $[Fe(VI)]_0$ = 500 μM.

4. Environmental Implications

This study discusses the critical role of secondary amines in enhancing Fe(VI)-based oxidation systems. By identifying Di and Py as high-performance activators (degradation kinetics accelerated by ~2-fold and 7-fold compared to Fe(VI) alone, respectively), the findings should enable reductions in Fe(VI) dosage and treatment time, thereby minimizing secondary sludge generation and chemical costs. The dominance of Fe(IV) over free radicals in pollutant degradation further reduces risks of toxic byproduct formation (e.g., halogenated organic compounds), aligning with safer water purification strategies. Importantly, the revealed negative correlation between the HOMO energy levels of secondary amines and their activation efficiency provides a molecular blueprint for designing eco-friendly amine ligands, guiding synthetic chemistry toward non-toxic, electronically tunable alternatives. The iron-amine complexation mechanism may also inspire low-carbon solutions that could convert nitrogen-containing waste compounds into Fe(VI) activators. Furthermore, the amine-coordination-mediated extension of Fe(IV) lifetime enhances pollutant mineralization efficiency, which is crucial for eliminating persistent micropollutants in aquatic environments.

It should be emphasized that due to the structural complexity of secondary amines, the impacts and underlying mechanisms of Fe(VI)-mediated pollutant degradation by secondary amines containing additional functional groups (e.g., -COOH, -OH) remain unclear. Further investigations into the fundamental mechanisms of introducing other functional groups into Fe(VI)-based pollutant oxidation systems are essential. Such studies will deepen the understanding of secondary amine-Fe(VI) interactions and strengthen the theoretical foundation for designing highly efficient secondary amine-based compounds to activate Fe(VI).

Acknowledgments

This work was supported by the National Natural Science Foundation of China (52070134, 52270075), Outstanding Youth Science Foundation of Sichuan Province Natural Science Foundation (2025NSFJQ0010), Litree Purifying Technology Co., Ltd. Project (2021H012). A.T. acknowledges the support of Politecnico di Torino. We would like to thank the Institute of New Energy and Low-Carbon Technology, Sichuan University, for Raman tests. We would like to thank the Analytical & Testing Center of Sichuan University for EPR measurement.

References

(1) Rougé, V.; Nguyen, P. T. T. H.; Allard, S.; Lee, Y. Reaction of Amino Acids with Ferrate(VI): Impact of the Carboxylic Group on the Primary Amine Oxidation Kinetics and Mechanism. *Environ. Sci. Technol.* **2023**, *57* (47), 18509–18518. https://doi.org/10.1021/acs.est.2c03319.

(2) Deng, Z. K.; Zhu, J. Y.; Zeng, C. Y.; Mu, R.; Ma, Y. F.; Zhang, Z. L. Highly Efficient Activation of Ferrate (VI) via Corncob Biochar Assisted by Electrochemistry for the Removal of Sulfamethoxazole from Water. *Chem. Eng. J.* **2024**, *484*, 149479. https://doi.org/10.1016/j.cej.2024.149479.

(3) Sharma, V. K.; Kazama, F.; Jiangyong, H.; Ray, A. K. Ferrates (Iron(VI) and Iron(V)): Environmentally Friendly Oxidants and Disinfectants. *J. Water Health* **2005**, *3* (1), 45–58. https://doi.org/10.2166/wh.2005.0005.

(4) Mao, Y.; Chen, Z.; Lu, Y.; Cao, K. F.; Wu, Y. H.; Hu, H. Y. Inactivation of Bacteria in Water by Ferrate(VI): Efficiency and Mechanisms. *Environ. Sci. Technol.* **2023**, *57* (49), 20893–20904. https://doi.org/10.1021/acs.est.3c05118.

(5) Qi, X. C.; Ding, L. Z.; Jian, C. Q.; Liu, R. T.; Liu, N.; Qu, D. Ferrate(VI) Oxidation of Substituted Nitrobenzene Compounds: Kinetics, Degradation, and Oxidized Products. *Chem. Eng. J.* **2024**, *488*, 150921. https://doi.org/10.1016/j.cej.2024.150921.

(6) Sharma, V. K.; Wang, J.; Feng, M.; Huang, C.-H. Oxidation of Pharmaceuticals by Ferrate(VI)–Amino Acid Systems: Enhancement by Proline. *J. Phys. Chem. A* **2023**, *127* (10), 2314–2321. https://doi.org/10.1021/acs.jpca.3c00134.

(7) Yates, B. J.; Zboril, R.; Sharma, V. K. Engineering Aspects of Ferrate in Water and Wastewater Treatment – a Review. *J. Environ. Sci. Health Part a* **2014**, *49* (14), 1603–1614. https://doi.org/10.1080/10934529.2014.950924.

(8) Tiwari, D. Ferrate(VI) a Greener Solution: Synthesis, Characterization, and Multifunctional Use in Treating Metal-Complexed Species in Aqueous Solution. In *Ferrites and Ferrates: Chemistry and Applications in Sustainable Energy and Environmental Remediation*; Sharma, V. K., Doong, R., Kim, H., Varma, R. S., Dionysiou, D. D., Eds.; ACS Symposium Series; American Chemical Society, 2016; Vol. 1238, pp 161–220. https://doi.org/10.1021/bk-2016-1238.ch007.

(9) Sun, X. H.; Feng, M. B.; Dong, S. Y.; Qi, Y.; Sun, L.; Nesnas, N.; Sharma, V. K. Removal of Sulfachloropyridazine by Ferrate(VI): Kinetics, Reaction Pathways, Biodegradation, and Toxicity Evaluation. *Chem. Eng. J.* **2019**, *372*, 742–751. https://doi.org/10.1016/j.cej.2019.04.121.

(10) Sharma, V. K.; Feng, M. B.; Dionysiou, D. D.; Zhou, H.-C.; Jinadatha, C.; Manoli, K.; Smith, M. F.; Luque, R.; Ma, X. M.; Huang, C.-H. Reactive High-Valent Iron Intermediates in Enhancing Treatment of Water by Ferrate. *Environ. Sci. Technol.* **2022**, *56* (1), 30–47. https://doi.org/10.1021/acs.est.1c04616.

(11) Shao, B. B.; Dong, H. Y.; Zhou, G. M.; Ma, J.; Sharma, V. K.; Guan, X. H. Degradation of Organic Contaminants by Reactive Iron/Manganese Species: Progress and Challenges. *Water Res.* **2022**, *221*, 118765. https://doi.org/10.1016/j.watres.2022.118765.

(12) Deng, Y.; Abdel-Shafy, H. I. Barriers to Ferrate(VI) Application in Water and

Wastewater Treatment. *Environ. Sci. Technol.* **2024**, *58* (7), 3057–3060. https://doi.org/10.1021/acs.est.3c09203.

(13) Wu, Y. H.; Wang, H. Z.; Du, J. S.; Si, Q. S.; Zhao, Q.; Jia, W. R.; Wu, Q. L.; Guo, W.-Q. Enhanced Oxidation of Organic Compounds by the Ferrihydrite–Ferrate System: The Role of Intramolecular Electron Transfer and Intermediate Iron Species. *Environ. Sci. Technol.* **2023**, *57* (43), 16662–16672. https://doi.org/10.1021/acs.est.3c05798.

(14) Guo, B. L.; Wang, J. Y.; Sathiyan, K.; Ma, X. M.; Lichtfouse, E.; Huang, C.-H.; Sharma, V. K. Enhanced Oxidation of Antibiotics by Ferrate Mediated with Natural Organic Matter: Role of Phenolic Moieties. *Environ. Sci. Technol.* **2023**, *57* (47), 19033–19042. https://doi.org/10.1021/acs.est.3c03165.

(15) Manoli, K.; Nakhla, G.; Ray, A. K.; Sharma, V. K. Oxidation of Caffeine by Acid-Activated Ferrate(VI): Effect of Ions and Natural Organic Matter. *AIChE J.* **2017**, *63* (11), 4998–5006. https://doi.org/10.1002/aic.15878.

(16) Wang, Y. P.; Xiao, Z. J.; Liu, Y. L.; Tian, W. J.; Huang, Z. S.; Zhao, X. N.; Wang, L.; Wang, S. B.; Ma, J. Enhanced Ferrate(VI) Oxidation of Organic Pollutants through Direct Electron Transfer. *Water Res.* **2023**, *244*, 120506. https://doi.org/10.1016/j.watres.2023.120506.

(17) Wang, Z. J.; Yang, X.; Du, Q.; Liu, T.; Dai, X.; Du, Y.; Zhang, H.; Zhou, P.; Xiong, Z. K.; Lai, B. Ferrate(VI)/Percarbonate for the Oxidation of Micropollutants: Interactive Activation and Release of Low-Concentration Hydrogen Peroxide for Efficient Electron Utilization. *J. Hazard. Mater.* **2024**, *469*, 134029.

https://doi.org/10.1016/j.jhazmat.2024.134029.

(18) Chen, X. J.; Bai, C. W.; Sun, Y. J.; Huang, X. T.; Zhang, B. B.; Zhang, Y. S.; Yang, Q.; Wu, J. H.; Chen, F. pH-Driven Efficacy of the Ferrate(VI)–Peracetic Acid System in Swift Sulfonamide Antibiotic Degradation: A Deep Dive into Active Species Evolution and Mechanistic Insights. *Environ. Sci. Technol.* **2023**, *57* (48), 20206–20218. https://doi.org/10.1021/acs.est.3c06370.

(19) Liu, M. Z.; Wu, N. N.; Li, X. Y.; Zhang, S. N.; Sharma, V. K.; Ajarem, J. S.; Allam, A. A.; Qu, R. J. Insights into Manganese(VII) Enhanced Oxidation of Benzophenone-8 by Ferrate(VI): Mechanism and Transformation Products. *Water Res.* **2023**, *238*, 120034. https://doi.org/10.1016/j.watres.2023.120034.

(20) Li, J.; Cao, J. C.; Jiang, M. J.; An, L. Q.; Zeng, G.; Mai, J. M.; Su, P.; Jing, B. H.; Feng, M. B.; Ao, Z. M.; Ma, J.; Yang, T. Role of Bipyridyl in Enhancing Ferrate Oxidation toward Micropollutants. *J. Hazard. Mater.* **2024**, *469*, 133982. https://doi.org/10.1016/j.jhazmat.2024.133982.

(21) Chen, K. Y.; Zhu, G. M.; Huang, X. J.; Huang, X. X.; Xu, Y. M.; Pang, H. L.; Luo, C. W.; Lu, J. S.; Zhang, Z. Q. New Insights into Degradation of Emerging Contaminants by S(IV)/Fe(VI) System in Neutral Water: Performance Enhancement, Reaction Mechanisms and Toxicity Assessment. *Sep. Purif. Technol.* **2024**, *328*, 125112. https://doi.org/10.1016/j.seppur.2023.125112.

(22) Wang, Z. J.; Du, Y.; Liu, T.; Li, J.; He, C. S.; Liu, Y.; Xiong, Z. K.; Lai, B. How Should We Activate Ferrate(VI)? Fe(IV) and Fe(V) Tell Different Stories about Fluoroquinolone Transformation and Toxicity Changes. *Environ. Sci. Technol.*

2024, *58* (10), 4812–4823. https://doi.org/10.1021/acs.est.3c10800.

(23) Zhang, Z.; Li, X.; Zhang, C.; Lu, S. H.; Xi, Y. N.; Huang, Y. C.; Xue, Z. Z.; Yang, T. Combining Ferrate(VI) with Thiosulfate to Oxidize Chloramphenicol: Influencing Factors and Degradation Mechanism. *J. Environ. Chem. Eng.* **2021**, *9* (1), 104625. https://doi.org/10.1016/j.jece.2020.104625.

(24) Sathiyan, K.; Wang, J. Y.; Williams, L. M.; Huang, C.-H.; Sharma, V. K. Revisiting the Electron Transfer Mechanisms in Ru(III)-Mediated Advanced Oxidation Processes with Peroxyacids and Ferrate(VI). *Environ. Sci. Technol.* **2024**. https://doi.org/10.1021/acs.est.4c02640.

(25) Tian, B. R.; Wu, N. N.; Liu, M. Z.; Wang, Z. Y.; Qu, R. J. Promoting Effect of Silver Oxide Nanoparticles on the Oxidation of Bisphenol B by Ferrate(VI). *Environ. Sci. Technol.* **2023**, *57* (41), 15715–15724. https://doi.org/10.1021/acs.est.3c03653.

(26) Shu, J.; Xu, X. P.; Zhang, Y. C.; Wang, K. M.; Zhu, Y. X.; Lian, X. R.; Wang, H. Y. Insight into the Mechanism of Ferrate(VI) Activation by Mineral Zincite for Carbamazepine Degradation: Role of Fe(V) Species and Free Radical Induction. *Chem. Eng. J.* **2023**, *473*, 145360. https://doi.org/10.1016/j.cej.2023.145360.

(27) Yang, T.; Mai, J. M.; Cheng, H. J.; Zhu, M. Y.; Wu, S. S.; Tang, L. Y.; Liang, P.; Jia, J. B.; Ma, J. UVA-LED-Assisted Activation of the Ferrate(VI) Process for Enhanced Micropollutant Degradation: Important Role of Ferrate(IV) and Ferrate(V). *Environ. Sci. Technol.* **2022**, *56* (2), 1221–1232. https://doi.org/10.1021/acs.est.1c03725.

(28) Baum, J. C.; Feng, M. B.; Guo, B. L.; Huang, C.-H.; Sharma, V. K. Generation of Iron(IV) in the Oxidation of Amines by Ferrate(VI): Theoretical Insight and Implications in Oxidizing Pharmaceuticals. *ACS ES&T Water* **2021**, *1* (8), 1932–1940. https://doi.org/10.1021/acsestwater.1c00156.

(29) Luo, C.; Feng, M. B.; Zhang, T. Q.; Sharma, V. K.; Huang, C.-H. Ferrate(VI) Oxidation of Pharmaceuticals in Hydrolyzed Urine: Enhancement by Creatinine and the Role of Fe(IV). *ACS ES&T Water* **2021**, *1* (4), 969–979. https://doi.org/10.1021/acsestwater.0c00255.

(30) Feng, M. B.; Baum, J. C.; Nesnas, N.; Lee, Y.; Huang, C.-H.; Sharma, V. K. Oxidation of Sulfonamide Antibiotics of Six-Membered Heterocyclic Moiety by Ferrate(VI): Kinetics and Mechanistic Insight into SO2 Extrusion. *Environ. Sci. Technol.* **2019**, *53* (5), 2695–2704. https://doi.org/10.1021/acs.est.8b06535.

(31) Frisch, M. J.; Trucks, G. W.; Schlegel, H. B.; Scuseria, G. E.; Robb, M. A.; Cheeseman, J. R.; Scalmani, G.; Barone, V.; Petersson, G. A.; Nakatsuji, H.; Li, X.; Caricato, M.; Marenich, A. V.; Bloino, J.; Janesko, B. G.; Gomperts, R.; Mennucci, B.; Hratchian, H. P.; Ortiz, J. V.; Izmaylov, A. F.; Sonnenberg, J. L.; Williams-Young, D.; Ding, F.; Lipparini, F.; Egidi, F.; Goings, J.; Peng, B.; Petrone, A.; Henderson, T.; Ranasinghe, D.; Zakrzewski, V. G.; Gao, J.; Rega, N.; Zheng, G.; Liang, W.; Hada, M.; Ehara, M.; Toyota, K.; Fukuda, R.; Hasegawa, J.; Ishida, M.; Nakajima, T.; Honda, Y.; Kitao, O.; Nakai, H.; Vreven, T.; Throssell, K.; Montgomery, J. A.; Peralta, Jr., J. E.; Ogliaro, F.; Bearpark, M. J.; Heyd, J. J.; Brothers, E. N.; Kudin, K. N.; Staroverov, V. N.; Keith, T. A.; Kobayashi, R.;

Normand, J.; Raghavachari, K.; Rendell, A. P.; Burant, J. C.; Iyengar, S. S.; Tomasi, J.; Cossi, M.; Millam, J. M.; Klene, M.; Adamo, C.; Cammi, R.; Ochterski, J. W.; Martin, R. L.; Morokuma, K.; Farkas, O.; Foresman, J. B.; Fox, D. J. Gaussian 16, Revision C.01. *Gaussian Inc, Wallingford CT* **2019**.

(32) Becke, A. D. Density-functional Thermochemistry. III. The Role of Exact Exchange. *J. Chem. Phys.* **1993**, *98* (7), 5648–5652. https://doi.org/10.1063/1.464913.

(33) Lee, C.; Yang, W.; Parr, R. G. Development of the Colle-Salvetti Correlation-Energy Formula into a Functional of the Electron Density. *Phys. Rev. B* **1988**, *37* (2), 785–789. https://doi.org/10.1103/PhysRevB.37.785.

(34) Grimme, S.; Ehrlich, S.; Goerigk, L. Effect of the Damping Function in Dispersion Corrected Density Functional Theory. *J. Comput. Chem.* **2011**, *32* (7), 1456–1465. https://doi.org/10.1002/jcc.21759.

(35) Grimme, S.; Antony, J.; Ehrlich, S.; Krieg, H. A Consistent and Accurate Ab Initio Parametrization of Density Functional Dispersion Correction (DFT-D) for the 94 Elements H-Pu. *J. Chem. Phys.* **2010**, *132* (15), 154104. https://doi.org/10.1063/1.3382344.

(36) Weigend, F. Accurate Coulomb-Fitting Basis Sets for H to Rn. *Phys. Chem. Chem. Phys.: PCCP* **2006**, *8* (9), 1057–1065. https://doi.org/10.1039/b515623h.

(37) Weigend, F.; Ahlrichs, R. Balanced Basis Sets of Split Valence, Triple Zeta Valence and Quadruple Zeta Valence Quality for H to Rn: Design and Assessment of Accuracy. *Phys. Chem. Chem. Phys.* **2005**, *7* (18), 3297–3305.

https://doi.org/10.1039/B508541A.

(38) Schäfer, A.; Huber, C.; Ahlrichs, R. Fully Optimized Contracted Gaussian Basis Sets of Triple Zeta Valence Quality for Atoms Li to Kr. *J. Chem. Phys.* **1994**, *100* (8), 5829–5835. https://doi.org/10.1063/1.467146.

(39) Schäfer, A.; Horn, H.; Ahlrichs, R. Fully Optimized Contracted Gaussian Basis Sets for Atoms Li to Kr. *J. Chem. Phys.* **1992**, *97* (4), 2571–2577. https://doi.org/10.1063/1.463096.

(40) Lu, T.; Chen, F. W. Multiwfn: A Multifunctional Wavefunction Analyzer. *J. Comput. Chem.* **2012**, *33* (5), 580–592. https://doi.org/10.1002/jcc.22885.

(41) Huang, Z. S.; Wang, L.; Liu, Y. L.; Jiang, J.; Xue, M.; Xu, C. B.; Zhen, Y. F.; Wang, Y. C.; Ma, J. Impact of Phosphate on Ferrate Oxidation of Organic Compounds: An Underestimated Oxidant. *Environ. Sci. Technol.* **2018**, *52* (23), 13897–13907. https://doi.org/10.1021/acs.est.8b04655.

(42) Lei, Y.; Yu, Y. F.; Lei, X.; Liang, X.; Cheng, S. S.; Ouyang, G. F.; Yang, X. Assessing the Use of Probes and Quenchers for Understanding the Reactive Species in Advanced Oxidation Processes. *Environ. Sci. Technol.* **2023**, *57* (13), 5433–5444. https://doi.org/10.1021/acs.est.2c09338.

(43) Li, G.; Jiang, J. C.; He, M. X.; Rao, D. D.; Zhang, J.; Sun, B. Enhancing Ferrate Oxidation of Micropollutants via Inducing Fe(V)/Fe(IV) Formation Needs Caution: Increased Conversion of Bromide to Bromate. *Environ. Sci. Technol.* **2023**, *57* (47), 18991–18999. https://doi.org/10.1021/acs.est.3c01395.

(44) Guo, Y.; Zhan, J. H.; Yu, G.; Wang, Y. J. Evaluation of the Concentration and

Contribution of Superoxide Radical for Micropollutant Abatement during Ozonation. *Water Res.* **2021**, *194*, 116927. https://doi.org/10.1016/j.watres.2021.116927.

(45) Niu, L. J.; Lin, J.; Chen, W. Z.; Zhang, Q.; Yu, X.; Feng, M. B. Ferrate(VI)/Periodate System: Synergistic and Rapid Oxidation of Micropollutants via Periodate/Iodate-Modulated Fe(IV)/Fe(V) Intermediates. *Environ. Sci. Technol.* **2023**, *57* (17), 7051–7062. https://doi.org/10.1021/acs.est.2c08965.

(46) Luo, M. F.; Zhou, H. Y.; Zhou, P.; Lai, L. D.; Liu, W.; Ao, Z. M.; Yao, G.; Zhang, H.; Lai, B. Insights into the Role of In-Situ and Ex-Situ Hydrogen Peroxide for Enhanced Ferrate(VI) towards Oxidation of Organic Contaminants. *Water Res.* **2021**, *203*, 117548. https://doi.org/10.1016/j.watres.2021.117548.

(47) Lee, H.; Lee, C.; Kim, J.-H. Response to Comment on "Activation of Persulfate by Graphitized Nanodiamonds for Removal of Organic Compounds." *Environ. Sci. Technol.* **2017**, *51* (9), 5353–5354. https://doi.org/10.1021/acs.est.7b01642.

(48) Li, B. B.; Guo, R. X.; Tian, J.; Wang, Z. Y.; Qu, R. J. New Findings of Ferrate(VI) Oxidation Mechanism from Its Degradation of Alkene Imidazole Ionic Liquids. *Environ. Sci. Technol.* **2021**, *55* (17), 11733–11744. https://doi.org/10.1021/acs.est.1c03348.

(49) Zong, Y.; Chen, L.; Zeng, Y. Q.; Xu, J.; Zhang, H.; Zhang, X. M.; Liu, W.; Wu, D. Do We Appropriately Detect and Understand Singlet Oxygen Possibly Generated in Advanced Oxidation Processes by Electron Paramagnetic Resonance

Spectroscopy? *Environ. Sci. Technol.* **2023**. https://doi.org/10.1021/acs.est.3c01553.

(50) Zhao, L. X.; Cheng, X. Y.; Wang, Z. X.; Zhang, E. Z.; Liu, Z. L.; Zhou, H. J.; He, L.; Guan, Q. Q. Generating High-Valent Iron-Oxo ≡FeIV=O Complexes by Calcium Sulfite Activation in Neutral Microenvironments for Enhanced Degradation of CIP. *Environ. Pollut.* **2023**, *336*, 122449. https://doi.org/10.1016/j.envpol.2023.122449.

(51) Son, Y. J.; Kim, S.; Leung, V.; Kawashima, K.; Noh, J.; Kim, K.; Marquez, R. A.; Carrasco-Jaim, O. A.; Smith, L. A.; Celio, H.; Milliron, D. J.; Korgel, B. A.; Mullins, C. B. Effects of Electrochemical Conditioning on Nickel-Based Oxygen Evolution Electrocatalysts. *ACS Catal.* **2022**, *12* (16), 10384–10399. https://doi.org/10.1021/acscatal.2c01001.

(52) Narku-Tetteh, J.; Muchan, P.; Saiwan, C.; Supap, T.; Idem, R. Effect of Side Chain Structure and Number of Hydroxyl Groups of Primary, Secondary and Tertiary Amines on Their Post-Combustion CO2 Capture Performance. *Energy Procedia* **2017**, *114*, 1811–1827. https://doi.org/10.1016/j.egypro.2017.03.1309.